The International Journal of Advanced Manufacturing Technology
https://doi.org/10.1007/s00170-025-16296-y

ORIGINAL ARTICLE

Effect of the printing orientation on the yield surface and its evolution reflecting plastic pre-deformation of additively manufactured stainless steel 316L

Ved Prakash Dubey[1,3] · Mateusz Kopec[1,3] · Dominika Przygucka[2] · Marzena Pawlik[3] · Paul Wood[3] · Zbigniew L. Kowalewski[1]

Received: 16 April 2025 / Accepted: 1 August 2025

Abstract
This study explores the influence of printing orientation on the yield surface characteristics and their evolution under plastic pre-deformation in additively manufactured (AM) stainless steel 316L produced via laser powder bed fusion (LPBF). Tubular specimens were fabricated in three orientations (XY, ZX, and *Z*) and subjected to multi-axial loading to experimentally determine initial and subsequent yield surfaces using a single-specimen probing approach. The yield surfaces were derived at two offset strain definitions (0.001% and 0.005%) and further analyzed after tensile pre-deformations of 0.35%, 0.5%, and 0.8%. Results revealed strong anisotropy in the AM specimens, with the *Z*-oriented samples displaying the lowest yield strength and most significant softening. In contrast, the XY and ZX orientations exhibited higher resistance to plastic deformation. The wrought SS316L showed superior mechanical performance. The evolution of yield surfaces highlighted the orientation-dependent hardening/softening mechanisms and directional stress redistribution. Electron backscatter diffraction (EBSD) analysis revealed that the microstructural anisotropy and grain morphology—particularly the presence of columnar grains in the *Z*-oriented samples—correlate strongly with the observed mechanical anisotropy and yield surface asymmetry.

Keywords Stainless steel · Yield surface · Additive manufacturing · Laser powder bed fusion melting (LPBF-M)

1 Introduction

Stainless steel 316L (SS316L) belongs to the materials of an austenitic structure. It is widely used in such industries as aerospace, medical, and energy due to its exceptional combination of mechanical properties, corrosion resistance, and biocompatibility [1]. These properties make it a preferred material for critical applications like implants, structural components, and chemical processing equipment. The low carbon content of SS316L minimizes carbide precipitation, enhancing its weldability and resistance to intergranular corrosion. Furthermore, SS316L exhibits excellent ductility and toughness across a broad temperature range, making it suitable for environments where mechanical stress and chemical reaction coexist [2]. In biomedical applications, SS316L is employed for manufacturing surgical tools and orthopaedic implants due to its non-reactive surface and superior strength. In the power engineering sector, it is used for components exposed to high-pressure and high-temperature conditions, such as heat exchangers and reactor vessels. Its combination of low thermal conductivity, high melting point, limited sensitivity to oxygen absorption, and high absorptivity in infrared also makes SS316L ideal for additive manufacturing (AM) techniques, such as laser powder bed fusion (LPBF), enabling the fabrication of intricate geometries and optimized designs tailored to specific applications [3].

Traditional manufacturing methods, including casting, forging, and machining, have been historically employed to process SS316L. However, these methods often result in material wastage and limitations in geometric complexity.

✉ Mateusz Kopec
mkopec@ippt.pan.pl

1 Institute of Fundamental Technological Research, Polish Academy of Sciences, Pawinskiego 5B, Warsaw 02-106, Poland

2 Faculty of Advanced Technologies and Chemistry, Military University of Technology, 00-908 Warsaw, Poland

3 Institute for Innovation in Sustainable Engineering, College of Science and Engineering, University of Derby, Derby DE22 1GB, UK

Published online: 16 August 2025

The emergence of AM has revolutionized the production of SS316L components. AM for SS316L encompasses different technologies such as powder bed fusion (PBF), directed energy deposition (DED), fused deposition modelling (FDM), and binder jetting (BJ) [4]. The selection of the appropriate printing technology and parameters is crucial for ensuring a successful process during which crack-free components with extremely low porosity can be manufactured [5]. Therefore, it is essential to apply optimized process parameters to achieve the required mechanical properties since they are strongly dependent on the AM process strategy applied [6]. LPBF involves selectively melting fine metal powders layer by layer using a high-energy laser, facilitating near-net-shape manufacturing and reducing material waste. Moreover, LPBF offers the flexibility to produce customized components with intricate internal structures that are challenging to achieve with conventional techniques [7]. Despite its advantages, LPBF introduces unique challenges, including residual stresses, anisotropic mechanical properties, and variations in microstructure. These factors significantly influence the mechanical behaviour of SS316L, including its yield strength, ductility, and overall performance. Addressing these challenges requires a comprehensive understanding of the material's mechanical properties and their dependence on the printing orientation and post-processing conditions.

The mechanical characterization of materials is still primarily performed using uniaxial testing methods in research and commercial facilities. Uniaxial tensile tests conducted on SS316L manufactured using selective laser melting (SLM) [8], directed laser deposition (DLD) [9], laser engineered net shaping (LENS) [10], and high-power direct laser deposition [11] have demonstrated superior mechanical properties in the horizontal and 45° orientations compared to the vertical orientation. One should highlight that uniaxial testing methods provide only limited data concerning the mechanical strength and damage of materials in a single direction, which does not simulate the real-world multiaxial stress conditions encountered by materials in most engineering applications. To fully understand all aspects of material's behaviour, such as initial texture or anisotropy, yield surface determination in the biaxial or triaxial stress space is important [12, 13]. Determination of the yield surface of SS316L is crucial for predicting its performance under complex loading conditions, especially in safety–critical applications such as pressure vessels, aerospace structures, and medical implants. Yield surface analysis enables the identification of anisotropy and directional dependencies in mechanical behaviour, which are particularly pronounced in additively manufactured materials. For LPBF-fabricated SS316L, the anisotropy in mechanical properties arises from the layer-by-layer building process, resulting in heterogeneous microstructures and residual stress distributions.

The yield strength of SS316L is a critical parameter dictating its performance in structural applications. For LPBF-fabricated components, the yield strength varies with printing orientation due to the anisotropic microstructure. Lavery et al. [14] reported yield strengths of 325 MPa and 415 MPa for samples printed along vertical and horizontal directions, respectively. Moreover, on post-processing treatment such as hot isostatic pressing (HIP), they demonstrated that it reduced anisotropy by homogenizing the microstructure and relieving residual stresses, achieving yield strength values of approximately 225 MPa in both directions.

Kumar et al. [15] examined the mechanical properties of SS316L produced via binder jetting (BJ) and LPBF, highlighting changes due to microstructural variations. The yield strength increased from 273 MPa (wrought) to 511 MPa and 430 MPa (LPBF) in vertical and horizontal printed specimens, respectively, due to fine cellular structures, while BJ exhibited a lower yield strength equal to 198 MPa in both printed directions due to higher porosity. These findings suggest that while LPBF enhances strength, it shows considerable anisotropy, whereas BJ SS316L leads to isotropy through microstructural advantages. This anisotropy necessitates a thorough understanding of the yield surface of AM SS316L, which describes the combination of stress states under which a material begins yielding itself.

Yield surface analysis has been extensively studied for isotropic and anisotropic materials. However, the available literature on the experimental identification of yield surface for additively manufactured stainless steel 316L is still limited. Somlo et al. [16] presented a computing attempt to determine yield surfaces for additively manufactured metals, austenitic stainless steel 316L and titanium alloy Ti-6Al-4 V, through crystal plasticity modelling. Although some experimental papers devoted to the identification of yield surface based on the uniaxial or biaxial tensile tests of the 316L stainless steel manufactured by selective laser melting could be found, they do not consider printing orientation [17, 18].

The experimental studies on yield surface identification for AM materials are also important from the modelling point of view. In the last decade, crystal plasticity has become an indispensable tool for establishing a connection between the microstructure of materials and their macroscopic mechanical strength [16]. It allows for a detailed description of the plastic deformation mechanisms of different AM materials, including SS316L. It should be stressed that despite having the same chemical composition, such material exhibits distinct mechanical properties as compared to its wrought form [1, 3, 9–11]. Therefore, it is of the highest importance to reveal the deformation mechanisms to further implement them into the material model to precisely predict its behaviour. At larger

scales, the heterogeneous microstructure of AM metals can be described using a homogeneous elastic–plastic material model [16]. An anisotropic yield function is usually employed to govern the plastic behaviour, and it can be determined through crystal plasticity simulations or directly from the experiments. There are numerous anisotropic yield criteria available, each utilizing quadratic or non-quadratic yield functions with varying numbers of adjustable parameters. Generally, the complexity and flexibility of a yield function increase with the number of parameters it incorporates. However, calibrating multiple parameters requires extensive experimental testing.

While significant progress has been made in understanding the mechanical behaviour of SS316L, gaps remain in the comprehensive yield surface characterization of LPBF-fabricated components, particularly concerning their anisotropy and the influence of printing orientation. This study aims to:

- Investigate the yield surface of LPBF SS316L with respect to three different printing orientations.
- Comparison of the yield surface of LPBF SS316L with that of wrought material.
- Determine the effect of plastic pre-deformation on the evolution of initial yield surface.

2 Materials and methods

The SS316L was additively manufactured by using the Renishaw AM 250 system with powder feedstock supplied by the same company. The Renishaw AM 250 is a laser powder bed fusion (LPBF) additive manufacturing system designed for high-precision metal 3D printing. It features a 200-W fibre laser, offering high precision with a 70-µm focal diameter and 1070-nm wavelength, along with a 250 × 250 mm build area, up to 300 mm deep. The inert atmosphere generation creates a vacuum before backfilling with high-purity argon, ensuring a high-quality build environment with minimal argon consumption and reduced oxidation. This system supports all qualified metals, including titanium and aluminium, making it ideal for aerospace and biomedical applications.

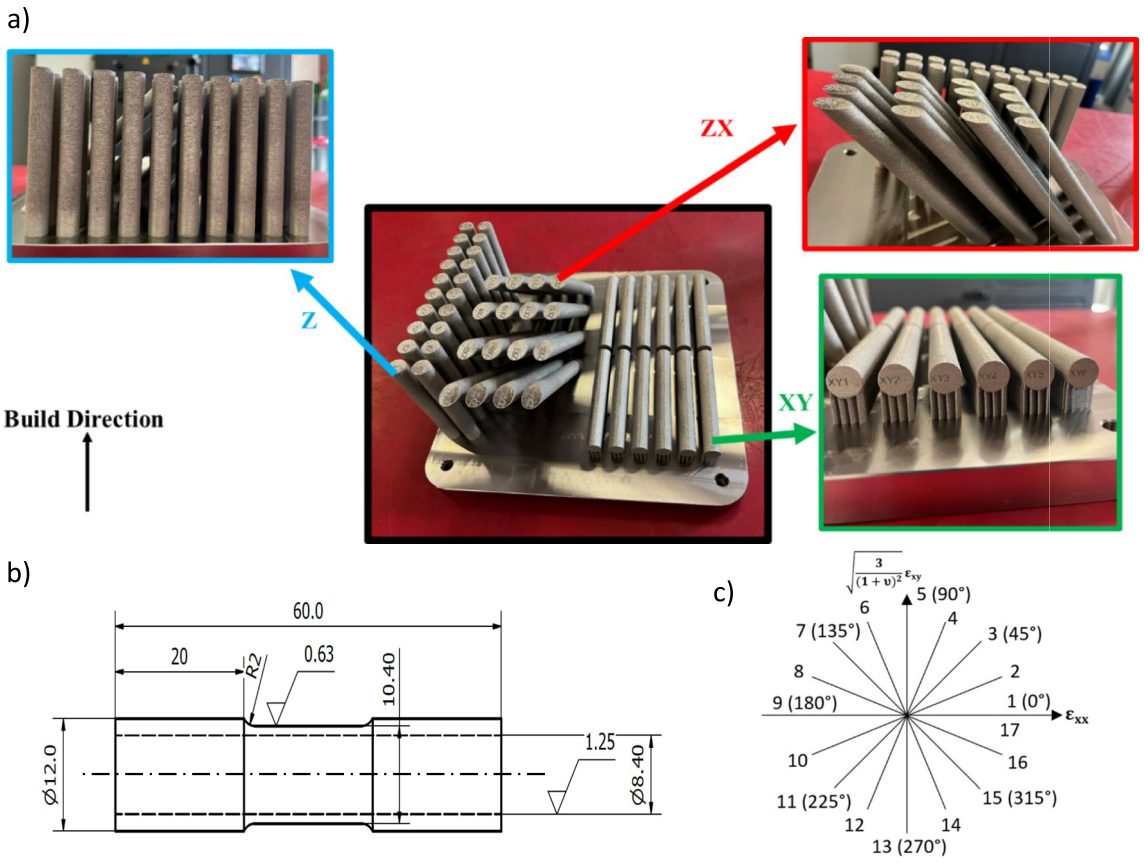

Fig. 1 Printing orientation of specimens on the build plate **a**; engineering drawing of the thin-walled tubular specimen for yield surface determination **b**; loading sequence of strain paths for yield points determination in the biaxial strain space **c**

Table 1 Process parameters applied during additive manufacturing

Region	Layer thickness [μm]	Hatch distance [mm]	Beam comp [mm]	Focal point [mm]	Power [W]	Point distance [μm]	Exposure time [μs]	Scan speed [mm/s]	Energy density [J/mm^3]
Volume fill hatch	50	0.11	0.025	0	195	60	80	750	47.27
Scanning strategy	Meander								

The round bars of diameter and length equal to 13 mm and 70 mm, respectively, were printed in three orientations (*Z* – vertical, XY – horizontal, ZX – 45°) (Fig. 1a) following the process parameters presented in Table 1. After the AM process, the as-built specimens were subjected to stress relief using a 470 °C soak for 6 h whilst still attached to the build plate following standards. The bars were then wire cut from the build plate and subsequently machined to achieve the thin-walled tubular specimen geometry (Fig. 1b). Both the inner and outer surfaces of the specimens were machined using the same turning parameters.

Mechanical testing was conducted using the MTS 858 servo-electrohydraulic biaxial testing machine, which has a maximum axial force capacity of ± 25 kN and a torque capacity of ± 100 Nm. All tests were performed at room temperature (23 °C). Initially, a uniaxial tensile test was carried out to evaluate the fundamental material properties, including the conventional yield strength (YS) $R_{0.2}$. The yield point was defined based on a 0.005% plastic offset strain, as determined from the stress–strain curve. Since this study employed a single-specimen methodology, the choice of a small plastic offset strain ensured that the accumulation of additional plastic strain from prior loading was minimal. This approach not only enhanced experimental cost efficiency but also provided a more accurate representation of the transition from elastic to plastic state. Consequently, a 0.005% plastic offset strain was adopted for yield surface determination across all cases. For subsequent experimental procedures, Vishay 120 Ω strain gauges were affixed to the midsection of the outer surface of the gauge region on thin-walled tubular specimens to monitor and control axial, shear, and hoop strain components (Fig. 1b). During yield probing, axial and shear strain components were recorded using a three-element 45° rectangular rosette (EA-05-125RA-120), whereas hoop strain measurements were taken with a linear pattern rosette (EA-13-062AK-120). A single-specimen methodology combined with a sequential probing technique under strain-controlled loading was employed to establish the initial yield surface for different material states (as-received and three printing orientations), encompassing 17 distinct strain paths. The loading sequence began and ended with tension in the same direction within the (ε_{xx}, $\sqrt{(3/(1+\nu)^2)}\varepsilon_{xy}$) strain plane (Fig. 1c), where ν represents Poisson's ratio. Subsequently, stress-controlled unloading was performed until force and torque returned to zero. The experimental investigations involved four stages:

(1) Determination of the basic mechanical properties of wrought and AM SS316L;
(2) Determination of the initial yield surfaces of wrought and as-printed SS316L;
(3) Introduction of tensile pre-deformation in the specimens at 0.35%, 0.5%, and 0.8% plastic strain;
(4) Determination of subsequent yield surfaces of the plastic pre-deformed specimens;
(5) microstructural analysis of undeformed and pre-deformed specimens.

The specimens were loaded to the desired value of plastic strain and then linearly unloaded to a zero-stress state. Subsequently, yield points were determined. Based on the stress–strain characteristic, the yield points for each path at 0.001% and 0.005% plastic offset strains were determined. The yield surface was obtained by fitting the experimental yield points with the Szczepinski anisotropic yield equation using the least squares method [19].

EBSD measurements were performed with a high-resolution Quanta 3D FEG scanning electron microscope system equipped with integrated EDS/EBSD capabilities, operating at 20 kV. Metallographic preparation included hot-mounting, followed by polishing with a Struers MD-Largo disc and 2-μm diamond suspension, and finishing with a Metrep® MD-Chem cloth and 0.04-μm colloidal silica solution.

3 Results and discussion

3.1 Results of the basic mechanical parameters of the material

The stress versus strain curves of wrought and three different printing orientations of SS316L are presented in Fig. 2. All tubular specimens were subjected to uniaxial tensile conditions at room temperature. Tensile strength is essential for

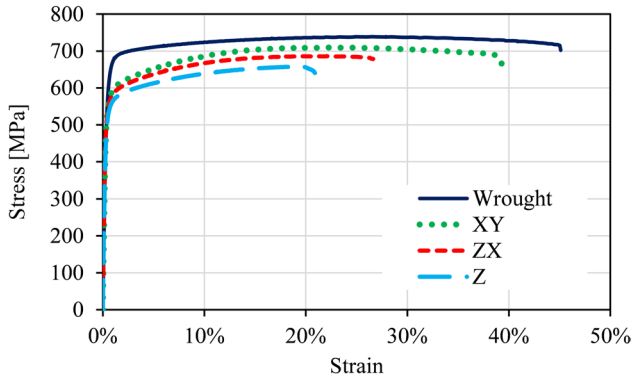

Fig. 2 Standard tensile characteristics of the additively manufactured and wrought SS316L

assessing the quality of the build part. The yield strength (0.2% YS), ultimate tensile strength (UTS), elongation at failure (EL), and Young's modulus (*E*) are presented in Table 2. The results show that the specimens printed in the horizontal direction exhibit slightly higher mechanical properties compared to those printed in the vertical and inclined orientations. The horizontal printing orientation resulted in a 9.5% increase in YS and an 8% increase in UTS compared to the vertical orientation. An increase of 82% in EL was also observed. These results align with previous studies [8] on the same SLM process and various printing orientations, as well as for components manufactured using LENS [10]. Notably, SLM-printed SS316L in the *Z* direction can exhibit elongation equal to more than 20%, depending on heat treatment, though the *Z* direction shows greater variability compared to the XY-printed specimens [20].

This anisotropy arises from the layer-by-layer manufacturing process, where the microstructural characteristics and interlayer bonding significantly impact mechanical performance [11]. In horizontally printed samples, the loading direction is parallel to the sliced layers, allowing the scanning tracks to act as reinforcing fibres, thereby improving mechanical strength. In contrast, when the orientation is vertical, the loading direction aligns perpendicular to the sliced layers, which results in lower tensile properties by weakening the metallurgical bonds between the layers.

In Table 2, the comparison of the mechanical properties of SS316L shows that LPBF-processed specimens of this work in XY, ZX, and *Z* orientations have lower tensile characteristics than those of the wrought one. Whereas these results are much higher in comparison with the reported data in the literature, where different techniques were used to produce the SS316L specimens.

A comprehensive microstructural analysis based on EBSD is presented in "Sect. 3.7" for all build orientations (XY, ZX, *Z*) as well as for the wrought condition. Previous studies have demonstrated that LPBF can induce preferred crystallographic orientation and texture along the build direction, influenced by scanning strategy; however, its effect can vary depending on processing parameters and material system [25–27]. A research study by Casati et al. [28] found no significant texture in LPBF-processed SS316L using a meander scanning strategy with a 67° rotation of the scanning direction after each layer. This rotation modifies thermal gradient directions, preventing texture formation and ensuring an isotropic polycrystalline structure. The additive manufacturing parameters used in this work are similar to the previous study. Therefore, the lack of a pronounced grain orientation in the samples suggests that variations in mechanical behaviour are primarily attributed to microstructural features. It is well known that microstructural defects such as micro-segregation, oxidation, inclusions, and melting defects are more prevalent at interlayer boundaries perpendicular to the build direction [29]. These defects act as stress concentrators, potentially reducing strength and ductility. Since interlayer boundaries in vertically printed samples are oriented orthogonally to the loading direction, stress concentration at these interfaces leads to earlier yielding, reduced strength, and lower elongation at failure. Conversely, in horizontal samples, these boundaries align

Table 2 Comparison of the mechanical properties of wrought and AM SS316L

		0.2% YS [MPa]	UTS [MPa]	EL [%]	E [GPa]
Wrought (current work)		610	740	45	178
XY (current work)		553	713	40	182
ZX (current work)		540	685	25	193
Z (current work)		505	660	22	185
Wire arc additive manufacturing [21]	XY	262	580	34	-
	Z	252	676	39	-
Electron beam powder bed fusion [22]	XY	396	652	31	-
	Z	334	572	29	-
Laser directed energy deposition [23]	XY	530	670	34	-
Cast [24]		262	552	55	-
Wrought [24]		170–310	480–623	30–40	-

parallel to the loading direction, minimizing stress localization and enhancing mechanical performance. Thus, this difference in the positioning of layer boundaries relative to the loading axis is a key factor in the anisotropic behaviour of LPBF-processed SS316L.

3.2 Effective mechanical parameters of the material tested under combined loading

Figure 3 presents the effective stress–strain curves, comparing the mechanical behaviour of wrought SS316L and LPBF-printed specimens in XY, ZX, and *Z* orientations under tension, tension–torsion, and pure torsion loading conditions. The effective stress is defined as the stress in a hypothetical state of deformation that is free of damage and is mechanically equivalent to the current state of deformation and damage. In wrought SS316L, the stress–strain responses for torsion and tension–torsion loading are close to each other, whereas the tensile curve deviates significantly (Fig. 3a), indicating different deformation mechanisms. A similar trend is observed in *Z*-oriented printed specimens (Fig. 3), suggesting that the building direction influences mechanical behaviour. The observed anisotropy in the mechanical response of wrought SS316L most likely did not originate from crystallographic anisotropy (as reported in "Sect. 3.7") but rather from differences in hardening behaviour, loading-path sensitivity, or microscale heterogeneities, which become evident under multiaxial loading.

In contrast, XY- and ZX-oriented specimens show minimal deviation between loading conditions at limited effective strain values, implying a more uniform response (Fig. 3b and c). These findings demonstrate that the same material can exhibit distinct mechanical responses depending on the loading conditions, primarily due to the initial anisotropy present in the material. This anisotropy affects stress accommodation, strain localization, and overall deformation behaviour, leading to variations in stress distribution under different loading paths. Understanding these differences is crucial for accurate prediction of material performance under complex loading scenarios, particularly in applications requiring multi-axial loading resistance.

3.3 Results of the material under tensile pre-deformation

The stress–strain and plastic strain curves of wrought SS316L and LPBF-printed SS316L specimens (in XY, ZX, and *Z* orientations) subjected to cyclic loading–unloading tensile tests for the purpose of plastic pre-strain (0.35%, 0.5%, and 0.8%) reveal key insights into their mechanical behaviour, as shown in Fig. 4. These results provide a detailed understanding of elastic–plastic deformation, strain recovery, and residual plasticity, essential for predicting material performance under repeated loading conditions.

As it can be observed from Fig. 4, all specimens demonstrate a smooth, continuous stress–strain response with a well-defined elastic–plastic transition. Each curve initially exhibits an elastic region followed by plastic deformation, where stress increases non-linearly. Whereas, after unloading to zero stress, the material does not return to its original strain but retains permanent plastic deformation (as seen by the shift in strain values for different curves). Upon unloading executed after different levels of plastic pre-strain, the wrought SS316L exhibits a strong elastic recovery with residual plastic strain (Fig. 4a and b), highlighting its superior work hardening and uniform deformation capability. The plastic strain accumulation per cycle is relatively low, suggesting greater microstructural stability and reduced

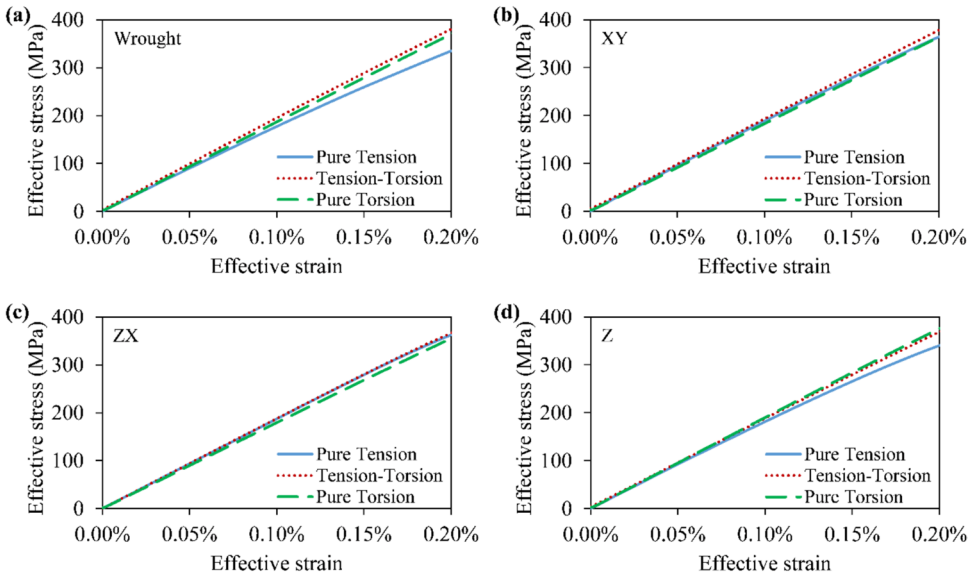

Fig. 3 Comparison of material characteristics of SS316L for different loading paths: pure tension; tension–torsion; and pure torsion on thin-walled tubular specimens

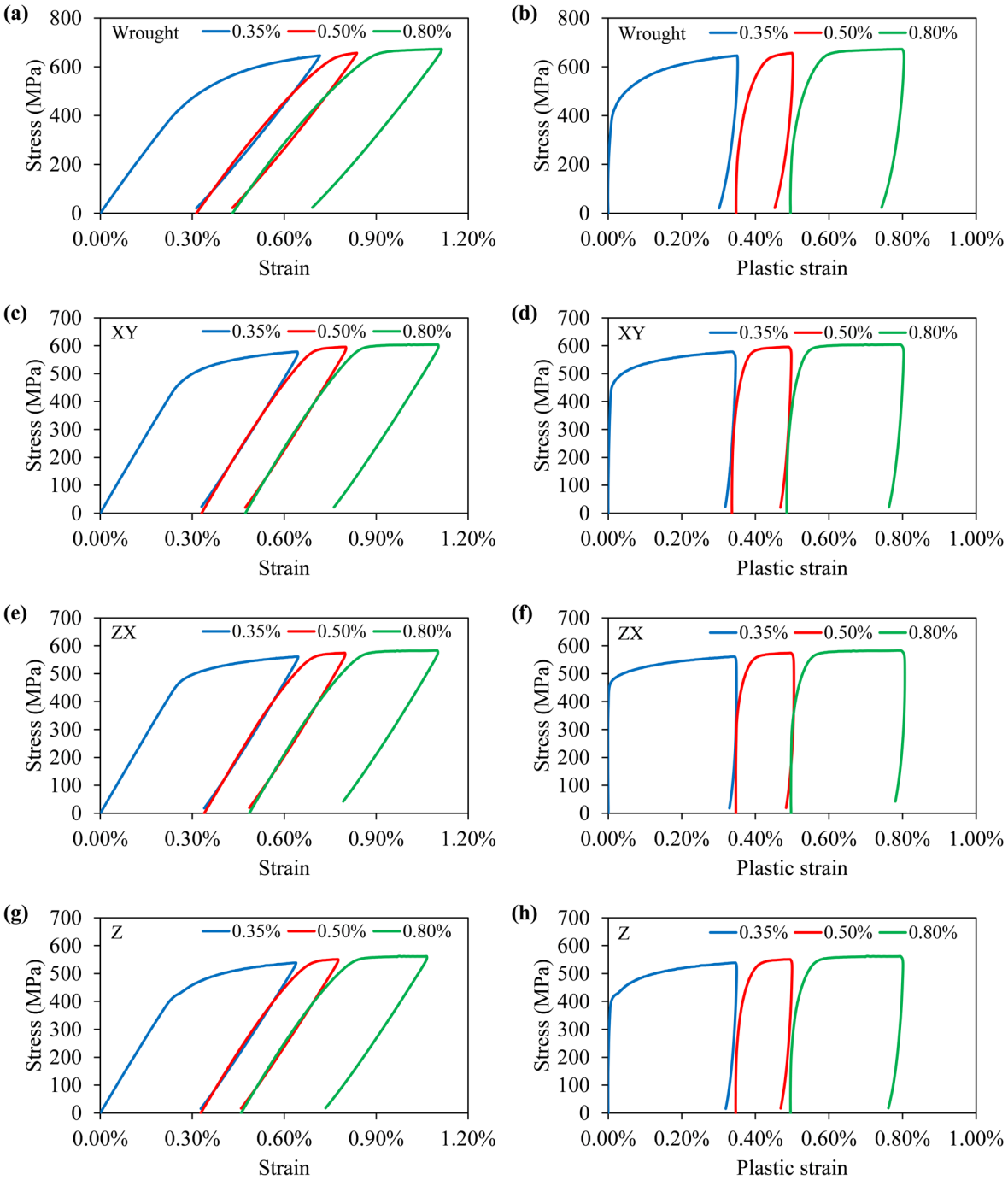

Fig. 4 Material response of tensile plastic pre-deformation and unloading after different values of plastic strain for wrought material **a**, **b** and those printed in XY **c**, **d**, ZX **e**, **f** and *Z* orientation **g**, **h**

dislocation pile-up, making it highly suitable for applications requiring excellent fatigue resistance. In contrast, the LPBF-printed specimens show notable differences in their cyclic stress–strain behaviour due to anisotropy and process-induced microstructural heterogeneities. The LPBF specimens display increased plastic strain accumulation per loading cycle with weak strain recovery potential, indicating a lower resistance to plastic deformation compared to the wrought specimen. The XY and ZX orientations show comparable mechanical behaviour, while the *Z* orientation exhibits significantly reduced mechanical performance, emphasizing the role of layer orientation and microstructural integrity in determining the cyclic stress–strain response. Compared to the wrought material, the LPBF specimens show a lower

yield point, suggesting a degree of microstructural softening due to the laser scanning strategy and heat accumulation.

3.4 Yield surface of SS316L in the as-received state

The stress–strain dependence for as-received wrought and as-printed SS316L was investigated in each of the 17 distinct strain paths (Fig. 1c) in a narrow plastic strain range to determine the yield points for further calculations of the yield surface. The yield points were determined using a loading–unloading method in various strain directions (being a different combination of axial and shear loads) via the specified offset strain approach. The loading and unloading paths showed negligible deviation from linearity across all directions, indicating minimal plastic deformation during the probing of the initial yield surface. The Poisson's ratio was used as 0.25 for calculations along all evaluated directions. The yield points of the as-received wrought and as-printed SS316L were determined at offset strain values of 0.001% and 0.005% for each stress path. After experimentally determining the yield points in various directions, ellipses were fitted via the least squares method using the Szczepinski anisotropic yield equation. The primary parameters of these ellipses are summarized in Table 3.

These ellipses representing yield surfaces (Fig. 5) demonstrate a clear dependence on the chosen yield definition. For the wrought SS316L, the yield surfaces at 0.001% and 0.005% offset strains (Fig. 5a) show a relatively symmetric and smooth distribution of yield points in the axial-shear stress plane. The axes ratio is nearly 1 for the yield surface at 0.005% offset strain. Whereas, the yield surfaces of LPBF-printed SS316L specimens (Fig. 5c, e, g) exhibit a slightly asymmetric distribution of yield points, with a broader spread along the axial stress axis compared to the shear stress axis. This suggests that the material exhibits higher resistance to axial deformation than that of the shear one. Additionally, the yield points of as-printed SS316L, determined at offset strain values of 0.001% and 0.005% (Fig. 5c, e, g), exhibit close proximity along the shear stress axis. In contrast, along the axial stress axis, the yield points for these two offset strain definitions are significantly separated, indicating a greater sensitivity to yield definition in axial loading conditions.

The initial yield surface at 0.005% offset strain is compared with the Huber-von Mises-Hencky (HMH) isotropic yield locus, which assumes material isotropy (Fig. 5b, d, f, h). The HMH isotropic yield surface is drawn by fixing the experimentally obtained yield point in tension. Figure 5b shows that the initial yield surface of wrought SS316L deviates more noticeably from the HMH isotropic yield locus, particularly in the shear stress region. This deviation confirms the presence of initial anisotropy in the as-received state of wrought SS316L. The observed initial anisotropy is attributed to distinct hardening behaviour in shear strength, which likely results from the manufacturing processes applied to the material.

Whereas, XY and ZX orientations exhibit a close agreement with the HMH locus (Fig. 5d and f), suggesting near-isotropic behaviour. In contrast, in the *Z* orientation (Fig. 5h), the yield surface deviates from the HMH isotropic yield locus, in the compressive and shear stress regions. This deviation suggests that the material's yielding in the *Z* orientation is influenced by the layered microstructure, which may introduce directional strengthening mechanisms such as grain boundary strengthening or texture effects. The *Z* orientation, being parallel to the build direction, may exhibit different deformation mechanisms compared to the XY and ZX orientations, leading to significant variations of yield points. Since the yield surface axis ratios of the printed materials (1.51 – XY, 1.58 – ZX, 1.44 – *Z*) are lower than the same ratio for the isotropic material according to the HMH yield condition (1.73), an occurrence of some initial anisotropy was confirmed.

Furthermore, the deviations from the HMH isotropic yield locus observed in the LPBF-printed specimens suggest that conventional yield criteria may not be sufficient to accurately predict the yield behaviour of AM materials. This highlights the need for the development of more advanced yield criteria that account for the anisotropic microstructure and directional dependence of mechanical properties in AM materials.

Yield surfaces obtained for 0.005% plastic offset strain of wrought and AM SS316L in three directions were compared in Fig. 5i. The yield stress at this offset strain was found to be 280 MPa (wrought), 372 MPa (XY), 370 MPa (ZX), 307 MPa (*Z*) in tension and − 301 MPa (wrought), − 385 MPa (XY), − 385 MPa (ZX), − 363 MPa (*Z*) in compression. It

Table 3 Ellipse parameters for the initial yield surface of SS316L for 0.005% plastic offset strain

	Centre (x_0, y_0) [MPa]	Rotation angle (∅) [radian]	Semi-axes (a, b) [MPa]	Axes ratio (a/b)
Wrought	− 12.63, 5.83	− 0.61	329.11, 312.65	1.05
XY	− 9.07, 3.14	0.03	400.34, 265.93	1.51
ZX	− 8.32, − 1.39	− 0.07	398.93, 251.89	1.58
Z	− 34.05, 7.60	− 0.04	367.12, 255.28	1.44

exposes the presence of tension–compression asymmetry in the initial state of materials. The yield stresses in torsion and reverse torsion were equal to 310 MPa, 260 MPa, 243 MPa, 261 MPa and − 299 MPa, − 250 MPa, − 246 MPa, − 247 MP a, respectively, for the same offset strain. It can be observed that the tensile yield strength at 0.005% plastic offset strain of wrought SS316L is lower than those of AM 316L, which is contrary to the results obtained for the conventional tensile strength (0.2% offset strain), reported in Fig. 2 and Table 2. This is due to the effect of the selected yield point definition, as Fig. 6 shows the stress–strain response of materials under tensile loading at smaller strain value. A close-up view of the tensile curves shows that the samples built using LPBF technology have a higher stress value at the very initial stage of elastic deformation in comparison to the wrought material (Fig. 6).

It can also be observed in Fig. 5i that the sizes of yield surfaces elaborated for LPBF specimens increased along tensile and compressive directions and shrunk in directions where torsion was applied, as compared to the specimen in wrought, as-received conditions. Such behaviour was probably associated with material anisotropy, and thus, different textures [30] and crystal structures [16]. The shape of yield surfaces for all printing orientations strongly indicates the texture presence [31]. However, it could be observed that the specimen built in the *Z*-orientation exhibits a notable shift of yield surface centre in the compression direction in comparison to that of other specimens (Table 3). It should be emphasized that based on the previous studies on additively manufactured materials, the anisotropic character of mechanical properties in AM SS316L is directly attributed to texture. However, as reported by Casati et al. [28], no significant texture was observed in the vertical and horizontal printed SS316L utilizing the LPBF process with a meander scanning strategy, incorporating a 67° rotation of the scanning direction after each layer. Therefore, considering the differences in mechanical properties due to the intrinsic anisotropy at different printing orientations, one should indicate an undoubted effect of microstructure, melt pool, and temperature gradient that are directly related to such issues. Recent studies by Liu et al. [32] have shown that a depth of the melt pool and remelting time interval can effectively control the grain size and dislocation density of SS316L manufactured by using dual-laser powder bed fusion. With the adoption of a 50-ms time interval, an increase of about 43 MPa in ultimate tensile strength could be achieved. During the LPBF-M process, the overlap of melt track boundaries could be found. The occurrence of such partial remelting between subsequent scanning tracks leads to the creation of a melting trajectory that exceeds the size of the laser spot due to the penetration depth being larger than the layer thickness [33]. Consequently, there is a remelting of the previous layer. This phenomenon enables grain growth in parallel or perpendicular orientations to the build direction in different dimensions, contributing to the anisotropic mechanical property [33, 34]. Furthermore, it has been observed that columnar grains grow in the direction of the temperature gradient, which also may affect the mechanical response of the material when it is deformed along the printing orientation.

Figure 7 presents the variation in the effective Young's modulus for wrought SS316L and LPBF-printed SS316L specimens in XY, ZX, and *Z* orientations across multiple loading paths within the axial-shear stress plane. As shown in Fig. 7, the results demonstrate a clear dependency of the Young's modulus on both the material processing route and the loading direction applied. For the wrought SS316L specimen, the effective Young's modulus varies between approximately 170 and 190 GPa, with notable oscillations across different loading directions. The highest stiffness is observed near 45° and 225°, whereas the lowest modulus values are recorded around 150° and 330°. This unexpected anisotropic behaviour in the wrought material, while more pronounced than in the LPBF-printed samples, may arise due to loading-path sensitivity or microscale heterogeneities introduced during manufacturing processes, which become evident under multiaxial loading.

Additionally, Fig. 7 shows that the XY- and ZX-oriented specimens exhibit a similar trend of variation of the effective Young's modulus as observed in the wrought specimen. An opposite trend was observed in the *Z*-oriented specimen. The XY- and ZX-oriented specimens maintain a relatively high Young's modulus (186–191 GPa) in the axial loading directions; however, they show a reduction near 120° and 300°. This behaviour suggests that the XY- and ZX-oriented specimens retain significant stiffness in the loading paths dominated by axial tension and compression but exhibit reductions in the effective stiffness under shear-dominated conditions. The *Z*-oriented specimens display a relatively low fluctuation, being within the range from 181 to 191 GPa. The stronger modulus variation suggests that the mechanical response in the LPBF-printed SS316L is more sensitive to the underlying grain orientation, defect distribution, and residual stress accumulation, which may result from the repeated laser scanning and subsequent cooling cycles.

3.5 Evolution of the initial yield surface with pre-deformation

The analysis of the subsequent yield surfaces in the axial-shear stress plane for both wrought and LPBF-printed SS316L in different orientations provides critical insights into the material's mechanical response under plastic deformation. The results presented in Fig. 8 provide the evolution of yield surfaces obtained for the as-received state of wrought SS316L and the as-printed specimens in XY, ZX,

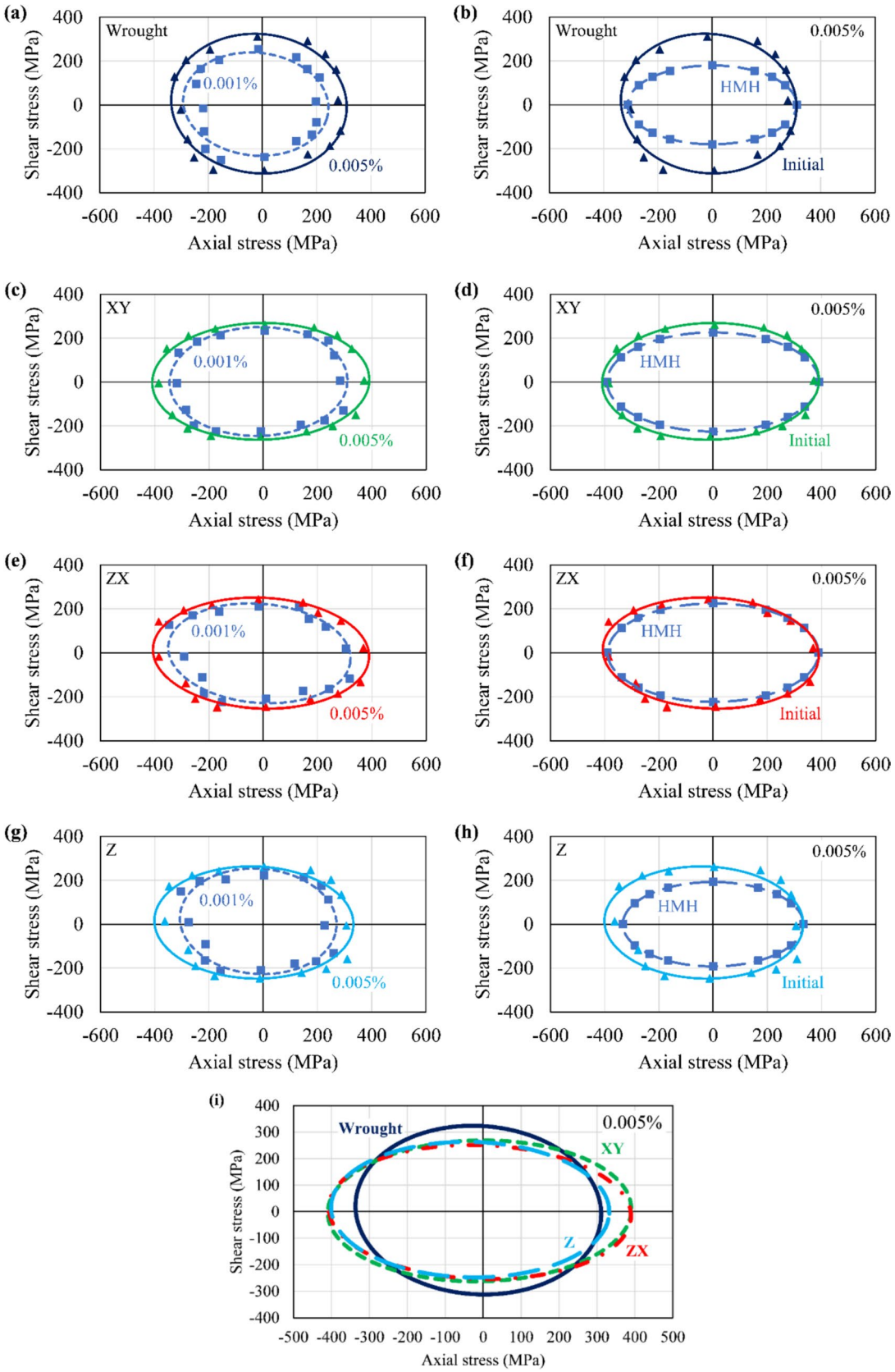
(a)
Wrought
0.001%
0.005%
(b)
Wrought
0.005%
HMH
Initial
(c)
XY
0.001%
0.005%
(d)
XY
0.005%
HMH
Initial
(e)
ZX
0.001%
0.005%
(f)
ZX
0.005%
HMH
Initial
(g)
Z
0.001%
0.005%
(h)
Z
0.005%
HMH
Initial
(i)
Wrought
0.005%
XY
Z
ZX
Shear stress (MPa)
Axial stress (MPa)

◂**Fig. 5** Yield surfaces of SS316L in the "as-received" state with yield points obtained for 0.005% and 0.001% plastic offset strains (**a, c, e, g**); initial yield surface (0.005% offset strain) of the SS316L compared with the Huber-von Mises-Hencky (HMH) isotropic yield locus (**b, d, f, h**); and comparison of the yield surfaces for three printing orientations and the same material in the as-received state for 0.005% plastic offset strain (**i**)

and *Z* orientations using LPBF. The yield surfaces changes were studied for three strain levels of the tensile plastic pre-deformation: 0.35%, 0.5%, and 0.8%. All yield surfaces were determined for 0.001% plastic offset strain. This method ensures an accurate representation of the plastic behaviour and its evolution due to prior deformation.

The initial yield surface evolution of the wrought SS316L specimen due to the tensile plastic pre-deformation (Fig. 8a) demonstrates a reduction of its dimensions, particularly in the compression and shear stress directions. Such contraction signifies a strain softening effect in directions orthogonal to the pre-deformation loading path, reflecting the kinematic character of softening. It means that while plastic deformation strengthens the material in the tensile direction, it reduces the yield stress in the transverse and shear directions, likely due to anisotropic dislocation interactions. Notably, at 0.35% plastic strain, the yield surface exhibits its smallest size, demonstrating an immediate softening effect, likely due to dislocation rearrangement. As the pre-strain increases to 0.5%, the yield surface expands nearly symmetrically, suggesting the activation of isotropic hardening mechanisms and the accumulation of statistically stored dislocations. At this stage, the yield stress surpasses that of the initial yield surface in the tensile direction. However, at 0.8% pre-strain, a slight contraction is observed compared to the 0.5% case, but the yield stress remains higher than that at 0.35%, indicating that strain hardening persists, though it may be partially offset by recovery or localized softening mechanisms. Additionally, the yield surfaces rotate, with the major axis orienting approximately 24° clockwise relative to the tensile stress direction applied, suggesting a redistribution of internal stresses and possible back stress effects.

The LPBF-printed SS316L specimen in the XY orientation (Fig. 8b) exhibits an anisotropic yield surface evolution following tensile plastic pre-deformation. The contraction of the yield surface is non-uniform, with the centre shifting slightly towards the positive axial stress direction at 0.35% plastic strain. The centre shift from the initial yield surface origin suggests a preferential softening opposite to the applied tensile stress, which may be attributed to the residual stress state and microstructural anisotropy inherent in LPBF processing. At 0.5% pre-strain, the yield surface becomes smaller, indicating enhanced directional softening, possibly due to instability or damage initiation in certain paths. Interestingly, after 0.8% pre-strain, the yield surface expands again, becoming the largest among all pre-strain levels. This suggests a transition to strain hardening as new dislocation networks are formed and stabilized. Despite this variation, all yield surfaces obtained after tensile pre-deformation remain smaller than the initial yield surface, emphasizing the persistent influence of microstructural anisotropy and potential texture-induced effects. Furthermore, the major axes of these yield surfaces rotate approximately 45° counter-clockwise with respect to the applied tensile pre-deformation direction, signifying a complex interaction between strain-induced softening and the anisotropic grain morphology of the LPBF-printed material.

The ZX-oriented LPBF-printed SS316L specimen (Fig. 8c) displays a comparable response to the XY orientation, particularly in terms of the rotational behaviour of the subsequent yield surfaces. The major axes of these yield surfaces also undergo a counter-clockwise rotation of approximately 30°. However, some notable differences are observed in these yield surfaces with increasing plastic pre-deformation. The yield surfaces after 0.35% and 0.5% plastic pre-deformation exhibit nearly identical characteristics, with higher yield stress levels than the initial yield surface along certain stress paths. This suggests that the material retains a substantial degree of strain hardening along specific directions at lower pre-strain levels. However, after 0.8% plastic pre-strain, the yield surface exhibits a noticeable contraction, becoming the smallest among all pre-strain levels. This reversal is indicative of localized softening, possibly due to microstructural degradation, dislocation recovery, or early onset of damage mechanisms that reduce the material's ability to sustain further plastic deformation. The distinct evolution of yield surfaces in this orientation highlights the influence of layer-wise grain structure and residual stress distribution, which govern the hardening and softening characteristics of LPBF-printed materials.

The yield surface evolution for LPBF-printed SS316L in the *Z* orientation (Fig. 8d) further emphasizes the influence of plastic pre-straining on material anisotropy. After tensile plastic pre-straining, a general softening trend is observed, with the lowest degree of this effect occurring after 0.5% plastic pre-deformation. At 0.35% plastic pre-strain, the yield surface contracts in an almost isotropic manner while slightly shifting towards the positive axial stress direction, indicative of uniform softening with a minor directional bias. With an increase of pre-strain to 0.5%, the yield surface expands compared to the 0.35% condition, demonstrating a transient hardening effect. However, at 0.8% plastic pre-strain, the yield surface closely resembles that at 0.35%, suggesting that strain hardening and subsequent recovery effects may balance each other out at higher plastic strains. These findings indicate that the *Z*-oriented LPBF specimens exhibit a complex interplay between strain hardening, residual stress relaxation, and microstructural anisotropy, which

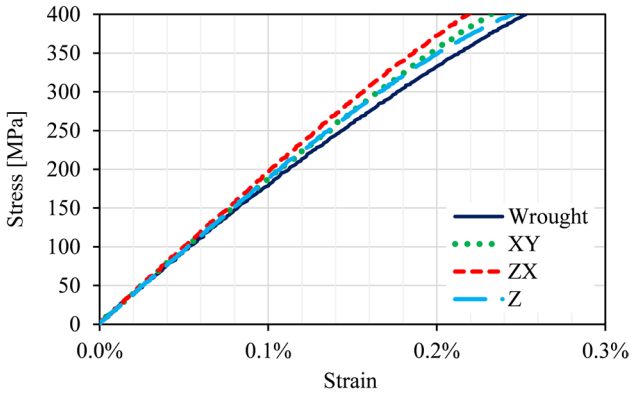

Fig. 6 Standard tensile characteristics of the additively manufactured and wrought SS316L for a limited strain range

collectively influence the mechanical response under plastic deformation.

Khan et al. [35] investigated the yield surfaces at 0.001% plastic offset strain after unloading through linear, bi-linear, and non-linear paths to zero stress from the 6% true tensile strain for a very low work hardening aluminium alloy (Al-6061-T6511) and showed contraction along the prior loading direction with plastic deformation. However, in another study by Khan et al. [36] on subsequent yield surfaces of a high work hardening aluminium alloy (annealed Al-1100) after unloading from 16% tensile pre-strain showed expansion, positive cross-effect, and translation in the pre-loading direction. Also, Ishikawa [37] determined the subsequent yield surfaces after complete unloading on an initially isotropic SUS 304 steel using 0.005% plastic offset strain. The results showed that approximately 0.4% tensile plastic pre-strain led to the contraction of the yield surface along the axial stress direction. Therefore, it can be concluded from the published results that the behaviour of the subsequent yield surface depends on the material type, pre-deformation level, and the definition of yield. In this study, the evolution of the initial yield surface of wrought SS316L displays a more predictable hardening–softening sequence, with a relatively symmetric yield surface evolution and a clear transition from softening to isotropic hardening. In contrast, the LPBF-printed specimens exhibit distinct yield surface shapes, orientations, and hardening/softening effects depending on the build direction.

The experimentally determined yield points for both the initial and plastically pre-deformed states of wrought SS316L and LPBF-printed SS316L in XY, ZX, and *Z* orientations were fitted using the Szczepinski yield function. The fitting procedure employed the least squares method to describe an elliptical approximation of the yield surface for each tested material condition. Table 4 presents the fitting errors, calculated as the sum of the squared distances between the experimentally obtained yield points and the corresponding points on the fitted yield surface. The results indicate that these fitting errors were consistently minimal across all cases, demonstrating a strong correlation between the experimental yield data and the derived elliptical yield surface approximation. The exceptionally low fitting errors not only validate the appropriateness of the Szczepinski yield function in describing the yield surface at different pre-strain levels but also highlight the reliability of the experimental measurements and data processing techniques employed in this study. The results suggest that the identified yield function parameters can be effectively incorporated into finite element modelling (FEM) frameworks for accurate simulations of the mechanical response of SS316L under complex loading conditions.

Figure 9 provides a comprehensive analysis of the evolution of the yield surface parameters for wrought SS316L and LPBF-printed SS316L in the XY, ZX, and *Z* orientations under varying levels of tensile plastic pre-deformation (0.35%, 0.5%, and 0.8% plastic strain). The major semi-axis of the yield surface, which represents the maximum yield strength of the material along a specific stress path, exhibits a general decreasing trend with the introduction of tensile plastic pre-strain across all material conditions (Fig. 10a). Initially, the major semi-axis values for the different materials vary significantly, with wrought SS316L exhibiting

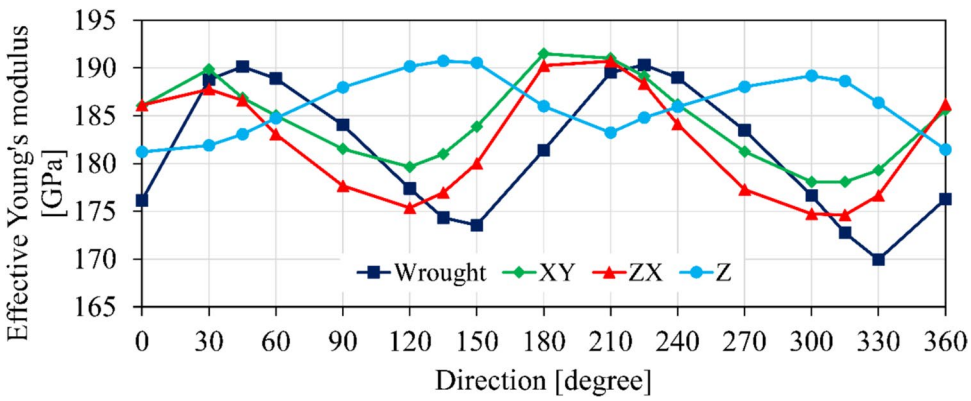

Fig. 7 The effective Young's modulus values of the SS316L in various loading directions of the strain plane considered

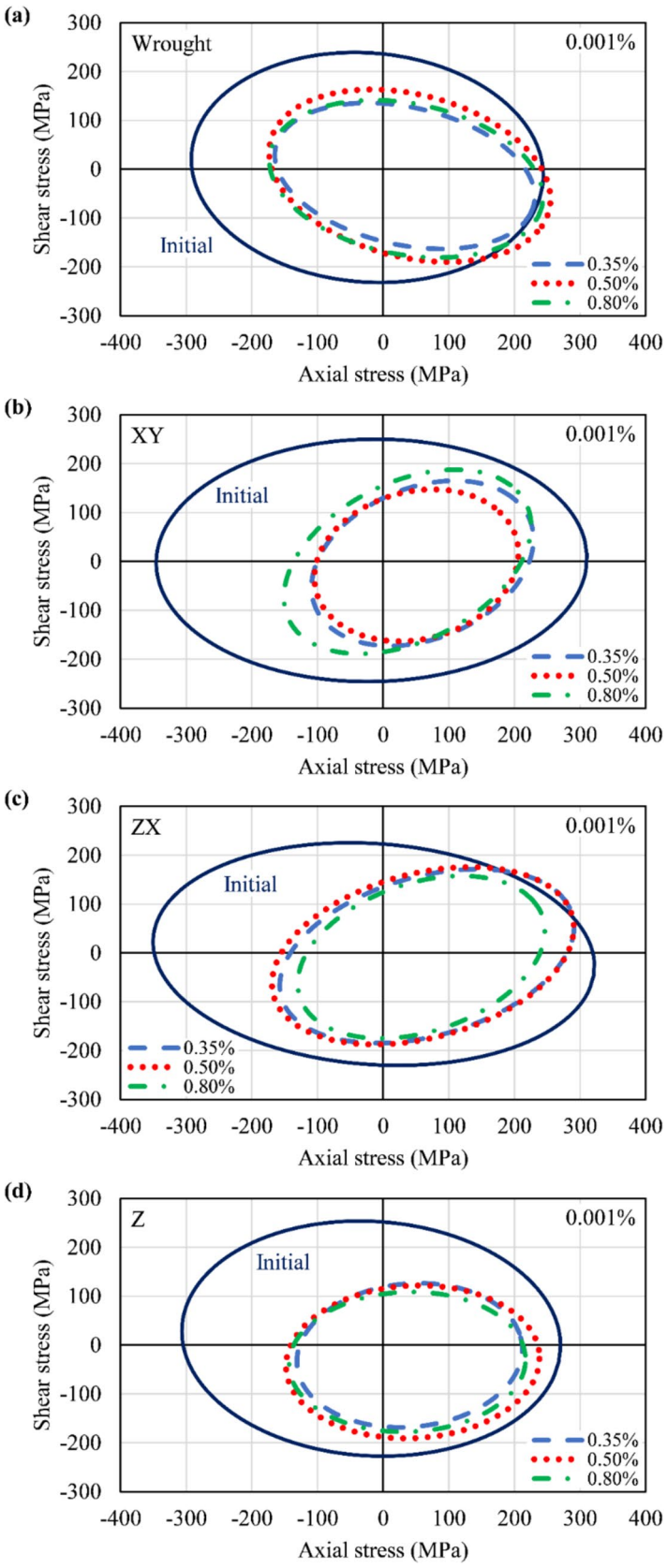

Fig. 8 Comparative analysis of the initial yield surfaces of the SS 316L with the yield surfaces of the same subjected to pre-deformation through the monotonic tension up to plastic pre-strain equal to 0.35%, 0.5%, and 0.8%, respectively

Table 4 The fitting errors associated with the yield surfaces for the material tested

Material	Initial	0.35% deformed	0.5% deformed	0.8% deformed
Wrought	0.329	0.420	1.32	0.873
XY	0.271	0.311	0.418	0.430
ZX	0.514	0.385	0.271	0.399
Z	0.658	0.589	1.04	0.669

the lowest value (270 MPa), while LPBF-printed specimens display higher initial values in the XY (328 MPa), ZX (338 MPa), and *Z* (290 MPa) orientations. With the introduction of plastic pre-strain, the major semi-axis decreases, particularly in the LPBF-printed specimens; the reduction is most pronounced. At 0.35% plastic strain, the XY-oriented specimen experiences the greatest decrease, approximately 41% lower than its initial value. As plastic pre-strain increases to 0.5%, the major semi-axis of the XY specimen continues to decline, while the wrought and other orientations exhibit a slight increase, indicating different strain hardening responses among orientations. However, after 0.8% plastic pre-strain, the trend reverses, with the major semi-axis stabilizing or slightly recovering in some cases. By this stage, the major semi-axis has reduced to 215 MPa in wrought SS316L, 222 MPa in XY, 206 MPa in ZX, and 180 MPa in *Z*. The relatively slower rate of decrease observed in wrought SS316L suggests that it undergoes a more stable softening process, while the LPBF-printed specimens exhibit a greater susceptibility to yield surface contraction, likely due to their distinct microstructural characteristics.

The minor semi-axis, which represents the minimum yield strength, follows a different pattern, as shown in Fig. 9b. It can be observed that initially all materials exhibit relatively similar minor semi-axis values, ranging between 226 and 248 MPa. However, upon applying 0.35% plastic pre-strain, all materials experience a significant decrease in their minor semi-axis values, reflecting softening effects. At 0.5% plastic pre-strain, a slight increase is observed in the wrought, ZX, and *Z* specimens, suggesting localized strain hardening effects. However, after 0.8% plastic pre-strain, a further decrease occurs. Whereas, in the XY orientation, the minor semi-axis remains nearly constant. Interestingly, at this stage, the minor semi-axis values for all materials converge within a narrow range of 143–151 MPa, indicating that despite initial differences in processing and orientation, all specimens exhibit similar minimum yield strengths after undergoing significant plastic deformation. This suggests that plastic pre-straining leads to a homogenization effect in yield surface characteristics, particularly in shear-dominated stress directions.

The axis ratio (*a*/*b*), which is the ratio of major to minor semi-axes and reflects the shape evolution of the yield surface, also varies with increasing plastic pre-strain, as shown in Fig. 9c. An axis ratio equal to 1.73 corresponds to the ideal Huber–von Mises–Hencky isotropic yield criterion. Deviations from this value signify directional hardening or anisotropic plastic flow behaviour. For wrought SS316L, the axis ratio increases from 1.16 in the initial state to 1.5 for 0.35% plastic pre-strain, suggesting early-stage anisotropic hardening due to dislocation structure evolution along preferred paths. This is followed by a slight decrease to 1.4 at 0.5% plastic pre-strain, and a small increase again to 1.42 at 0.8% plastic pre-strain. Such minor oscillations are likely attributed to the balance between strain-induced alignment of microstructural features and homogenisation effects due to progressive plastic deformation. In wrought material, with

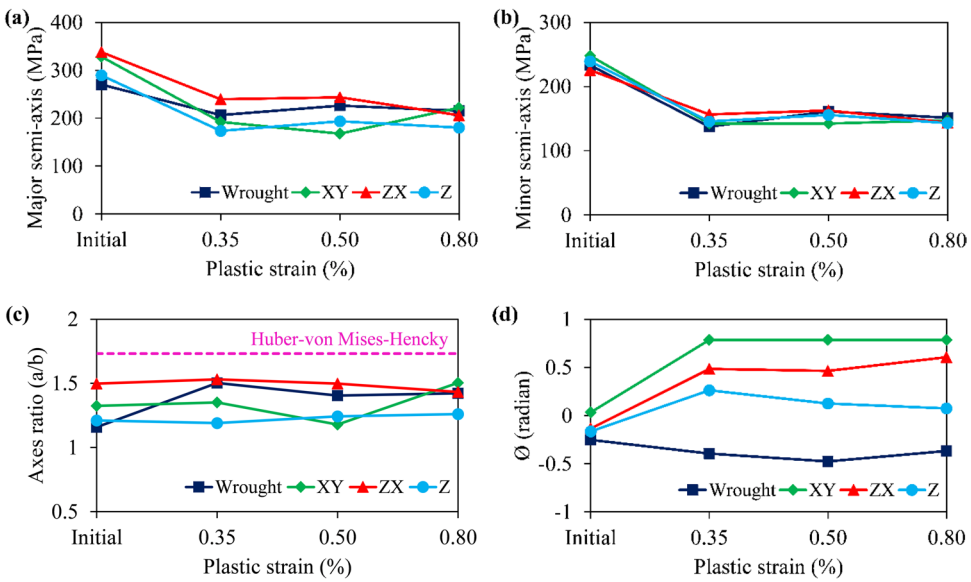

Fig. 9 Variation of the yield surface parameters of SS316L due to pre-deformation by monotonic tension up to plastic strain equal to: 0.35%, 0.5%, and 0.8%, respectively

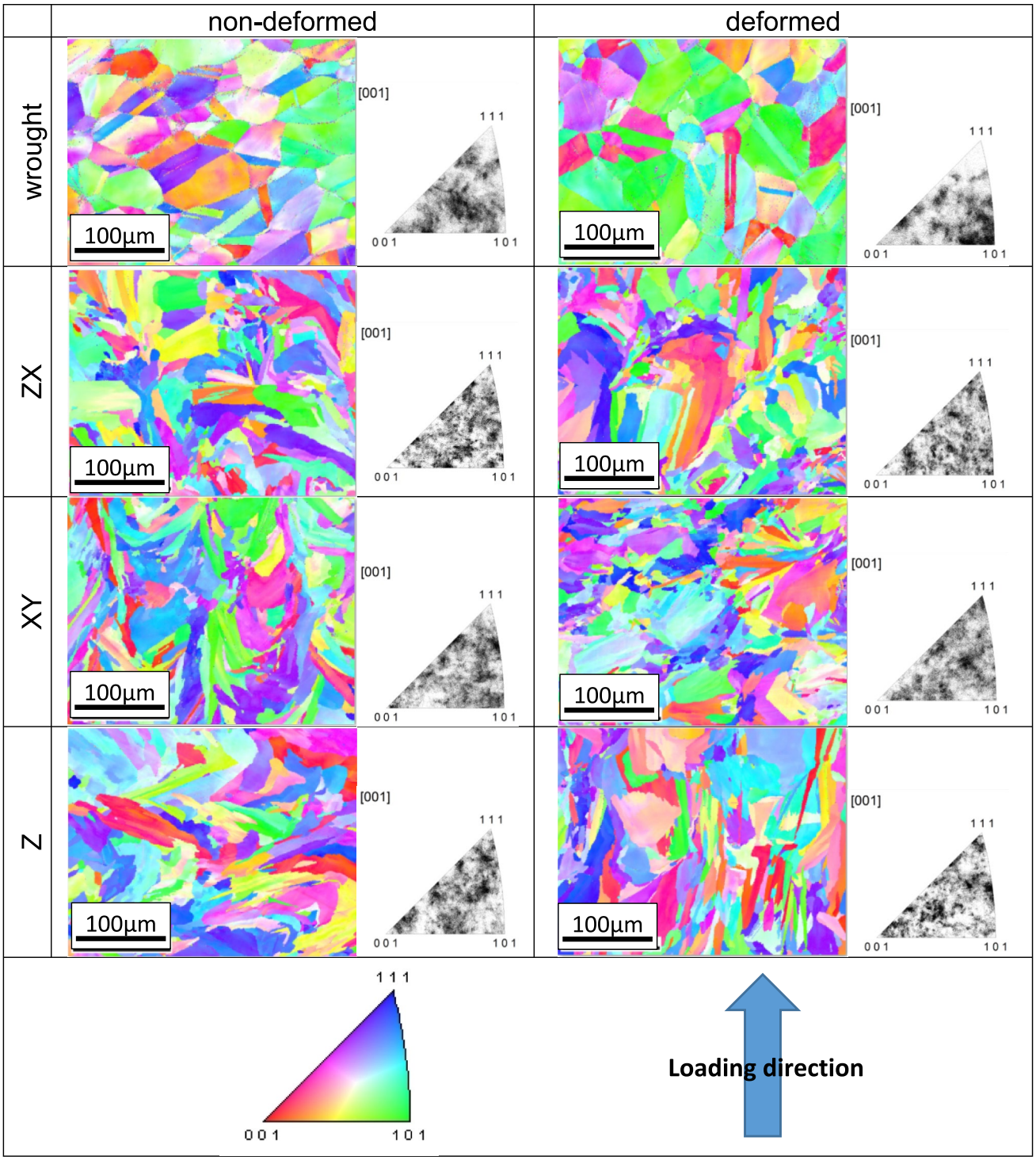

Fig. 10 IPF maps of SS316L specimens

its equiaxed grain structure and lack of strong texture, the anisotropy evolution is moderate and stabilizes with strain.

In contrast, the LPBF-XY orientation shows a non-monotonic behaviour, with an initial axis ratio of around 1.34 (initial and 0.35% plastic pre-strain), followed by a notable drop to 1.18 at 0.5% plastic pre-strain, and then a sharp rise to 1.5 at 0.8% plastic pre-strain. This behaviour reflects the strong textural and microstructural anisotropy introduced by the LPBF process, which makes the material more sensitive to the strain path and deformation history. The drop at 0.5%

likely indicates a temporary strain-induced softening or texture realignment, possibly due to activation of secondary slip systems or local yielding in less favourable crystallographic directions. The subsequent increase to 1.5 could be due to the development of directional hardening in dominant slip systems as the deformation becomes more localized along structurally preferred orientations.

The LPBF-ZX and LPBF-*Z* orientations exhibit relatively stable axis ratios of approximately 1.48 and 1.23, respectively, throughout the plastic pre-straining process, indicating a more consistent anisotropic response and less sensitive to evolving plasticity mechanisms in these orientations. Notably, the axis ratio for all tested materials remains lower than the theoretical value of 1.73 for the perfect Huber–von Mises–Hencky isotropic yield surface, indicating significant anisotropic effects in both wrought and LPBF-printed SS316L.

The evolution of the yield surface orientation, represented by the rotation angle ($\emptyset$), reveals important differences between wrought and LPBF-printed SS316L, as shown in Fig. 9d. The angle $\emptyset$ is measured from the axial stress direction (x-axis) to the major semi-axis of the fitted elliptical yield surface. It provides insight into directional hardening behaviour and internal anisotropy induced by plastic deformation. For wrought SS316L, the major semi-axis undergoes a progressive clockwise rotation (negative $\emptyset$) as the tensile plastic pre-strain increases, as evidenced by an increasing negative rotation angle, reaching approximately − 0.4 radians at 0.8% plastic strain. This behaviour suggests that plastic deformation induces a systematic reorientation of the yield surface, likely due to evolving dislocation structures and internal back stresses.

In contrast, LPBF-printed specimens show a markedly different response. Both XY and ZX orientations demonstrate a progressive counter-clockwise rotation (positive $\emptyset$), reaching values as high as 0.79 radians (~ 45°) in the XY orientation after plastic pre-straining. This significant reorientation of the yield surface reflects the strong directional microstructural features introduced during the plastic deformation, which is explained in details in "Sect. 3.7". The *Z*-oriented LPBF sample displays a smaller and more stable rotation trend, with $\emptyset$ remaining close to zero after an initial slight increase. This suggests that the evolution of the yield surface orientation is less pronounced along the build direction or possibly compensated by competing microstructural effects. Notably, the yield surface in some cases (e.g., initial LPBF-XY or LPBF-*Z* at 0.8% plastic strain) appears nearly aligned with the principal stress axes ($\emptyset \approx 0$). These instances, however, are not contradictory but represent specific points where anisotropic hardening does not induce a measurable rotation. Such behaviour reflects the complex interplay between strain path, microstructural anisotropy, and deformation history.

The anisotropic nature of the LPBF specimens leads to significant variations in major and minor semi-axes evolution, axes ratio trends, and yield surface rotation. These findings highlight fundamental differences in the mechanical response of conventionally processed and additively manufactured SS316L, providing crucial insights into their strain-hardening/softening behaviour and anisotropic plasticity.

Although the yield surface concept is commonly known, the experimental identification of yield surfaces for additively manufactured materials can be treated as a relatively new approach used in mechanics to characterise the material behaviour subjected to complex loading in stress states separating the elastic and plastic ranges [30, 38, 39]. One should emphasize that research in this area is mainly limited to numerical investigations through crystal plasticity [30, 38] and anisotropic [39, 40] models. Even though experimental data is used to validate or calibrate the model, it is mainly based on the uniaxial tensile test results. The approach presented in this research is thus important as it provides the experimental data for AM SS316L for which the yield surfaces were determined for three different printing orientations. Future studies should involve the combination of numerical and experimental approaches to establish a new model, which could be validated through data obtained in this research.

3.6 Yield definition influence on the yield surface dimensions

The definition of yield, especially the selection of the plastic offset strain (e.g., 0.001% vs. 0.005%), has a crucial impact on the determination and interpretation of the yield surface dimensions in AM SS316L. In this study, two yield definitions were employed to explore their influence on the yield surface for specimens fabricated using LPBF in three orientations (XY, ZX, *Z*) and compared with wrought SS316L. The difference in offset strain directly affects the measured yield points, which serve as the basis for constructing the yield surfaces in axial-shear stress space.

At the lower offset of 0.001%, the yield surfaces capture the very initial plastic response of the material. This early-stage yielding is more sensitive to intrinsic anisotropies induced during the LPBF process, such as directional grain growth, residual stresses, and layer-wise heterogeneities. Consequently, the yield surfaces determined at 0.001% are generally smaller and more irregular in shape. For example, in the *Z*-oriented LPBF specimens, the yield points were significantly separated along the axial direction while remaining closely clustered along the shear axis, indicating a strong directional dependence. This reveals how early plastic deformation is more likely to initiate in certain directions due to microstructural features, such as columnar grain

growth aligned with the build direction or weaker interlayer bonding.

On the other hand, yield surfaces constructed at 0.005% offset strain showed a noticeable expansion along the principal stress directions and were more regular in shape. This larger offset allows for a small amount of plastic deformation before yield is defined, thereby smoothing out minor local effects and making the yield surface less sensitive to microstructural irregularities. While this approach may slightly obscure the earliest stages of plasticity, it provides a more stable and consistent representation of the material's yield behaviour under multiaxial loading. For example, LPBF-printed XY and ZX specimens showed better agreement with the idealized Huber–von Mises–Hencky (HMH) isotropic yield locus at 0.005%, indicating that the isotropic effects are partially averaged out or less dominant at this higher offset.

The impact of yield definition is also reflected in the axis ratio and orientation (rotation angle) of the fitted elliptical yield surfaces. At 0.005% offset, the wrought material displayed nearly symmetric yield surfaces (axis ratio ≈ 1.05). On the other hand, the LPBF specimens, particularly in the ZX and XY orientations, exhibited higher axis ratios (1.51–1.58), pointing to anisotropy. These ratios differed more at the smaller offset, reinforcing the observation that isotropy is more evident when plasticity is defined closer to its onset. Furthermore, the centre of the yield surfaces shifted depending on the yield definition and orientation, especially in the *Z*-direction samples, which exhibited notable asymmetry and off-centre yield surfaces even at 0.005%.

One should highlight that the definition of the yield point plays a pivotal role in determining the dimensions and shape of the yield surface. A smaller offset strain reveals the early isotropic plastic behaviour and highlights the influence of microstructure, while a larger offset yields a more generalized view of the material's plastic response. For LPBF-manufactured materials, where directional effects are inherent, the chosen yield definition not only affects the quantitative results but also the qualitative understanding of plasticity and mechanical performance under complex loading. Thus, accurate yield surface characterization in AM materials requires careful consideration of the yield definition to ensure that both the anisotropy and its practical implications are properly captured.

3.7 Microstructural observations

The microstructural observations of wrought and AM SS316L stainless steel specimens were examined using EBSD. It enabled a quantitative assessment of grain boundary character, misorientation distribution, and grain morphology. Such observation revealed deformation mechanisms and were subsequently correlated with anisotropic mechanical behaviour observed during complex loading.

The inverse pole figure (IPF) maps generated via EBSD provide spatially resolved crystallographic orientation data, which were used to assess the microstructural anisotropy and the potential presence of texture in both wrought and LPBF-fabricated SS316L specimens (Fig. 10). These maps are presented for both non-deformed and tensile pre-deformed (0.8% plastic pre-strain) states of each material condition (wrought, XY, ZX, and *Z* orientations). All maps are indexed with respect to the loading axis.

The IPF maps of the wrought SS316L in both undeformed and deformed states present a random distribution of grain orientations with no specific texture. Grains exhibit an equiaxed morphology, typically associated with isotropic mechanical behaviour. Grain boundaries are smooth and uniformly distributed, with no evidence of directional grain elongation. This microstructural uniformity is reflected in the nearly circular initial yield surface and minimal evolution upon plastic pre-straining, as the deformation mechanisms remain consistent in all loading directions. After deformation, the IPF map of the wrought specimen revealed slight orientation changes within individual grains, indicative of lattice rotation during plastic deformation. However, no pronounced texture evolution or preferred orientation development was observed, suggesting that the deformation was homogeneously accommodated through intragranular slip rather than texture sharpening or twinning. These observations are consistent with the moderate rotation of the yield surface major axis (~24°) and symmetric hardening behaviour seen experimentally.

Although the EBSD analysis (Fig. 10) confirms that the wrought SS316L exhibits an isotropic grain structure, the mechanical response showed mild anisotropy at small plastic strains. This is evident from the differences in effective stress–strain curves observed under pure tension, pure torsion, and combined tension–torsion loading paths (Fig. 3a), as well as from the deviation of the initial yield surface from a perfect Huber–von Mises–Hencky isotropic yield surface (Fig. 5b). The observed anisotropy is not attributed to texture or directional grain elongation, but rather to the material's response under multiaxial loading conditions. Possible contributing factors include path-dependent hardening (e.g., latent hardening effects), non-associative flow behaviour, and microstructural heterogeneities such as dislocation structures or residual stresses, which may influence the onset of plasticity but are not captured in EBSD scans. Therefore, while the material is microstructurally isotropic, it exhibits a degree of mechanical anisotropy that becomes apparent under different loading conditions in the early stages of plastic deformation.

In the XY-oriented specimens, the IPF maps in the undeformed state reveal a fine-grained microstructure with nearly equiaxed grains and minor preferential alignment along certain crystallographic directions, likely due to the influence of the layer-wise melt pool solidification. Grain morphology is uniform; although, some elongation is occasionally observed parallel to the scanning direction, reflecting localized thermal gradients and epitaxial growth at melt track boundaries [28, 32]. Upon tensile pre-deformation, the IPF maps indicate an increase in intra-grain misorientation and mild grain rotation, particularly within larger grains. This is indicative of plastic strain accumulation through dislocation activity. No significant grain boundary migration or recrystallisation was observed, which aligns with the low-temperature nature of LPBF processing and the absence of post-processing heat treatment beyond stress relief. Notably, despite the absence of strong texture, the deformation-induced orientation changes lead to a pronounced rotation of the yield surface (up to ~ 0.79 radians), highlighting the sensitivity of the mechanical response to microstructural anisotropy introduced through processing.

The ZX-oriented samples, representing a 45° inclination relative to the build platform, show a more heterogeneous grain structure in the IPF maps. The undeformed state exhibits both equiaxed and elongated grains, with elongation occurring diagonally relative to the scan vectors. This mixed morphology suggests the interaction of multiple melt pool orientations and thermal gradients along the diagonal plane of building. After deformation, grains display increased fragmentation and notable internal orientation gradients, especially in elongated grains. Such observations indicate localised plastic deformation through dislocation cell formation and subgrain development. While a distinct texture is still absent, the heterogeneous grain structure contributes to non-uniform strain accommodation, which correlates with the observed anisotropic evolution of the yield surface—especially the stable axis ratio and moderate yield surface rotation (~ 30°).

The *Z*-oriented specimens, built vertically, demonstrate the most pronounced anisotropy in grain structure, as evidenced in the IPF maps [28, 31]. The undeformed microstructure consists of long columnar grains aligned along the build direction (parallel to the loading axis during testing). This alignment is the direct consequence of thermal gradients and solidification direction in the LPBF process. Columnar grains span multiple layers and are occasionally intersected by melt pool boundaries, suggesting partial remelting and epitaxial grain growth between subsequent layers [33, 34].

Following plastic pre-deformation, the IPF maps show localised intragranular misorientation bands aligned perpendicular to the loading axis, indicative of planar slip and dislocation pile-up within columnar grains. However, unlike in the XY and ZX samples, the orientation change is less pronounced, and no evidence of significant grain refinement or recrystallisation is visible. The persistence of columnar grain morphology even after plastic straining suggests limited capacity for dislocation cross-slip or dynamic recovery, contributing to the lower ductility and higher tendency for strain localisation.

The EBSD-derived misorientation statistics, shown in Fig. 11, were further summarised in Table 5 to provide insight into the deformation mechanisms. Grain boundaries were categorised based on misorientation angles: low-angle grain boundaries (LAGBs, 2°–15°) and high-angle grain boundaries (HAGBs, > 15°). One should highlight that the fraction of HAGBs was dominant across all specimens, with values ranging between 59.8 and 74.3%. This prevalence suggests that the microstructures are largely composed of recrystallised or well-annealed grains with relatively high resistance to dislocation transmission, particularly in the wrought condition.

For the as-built LPBF specimens, the fraction of LAGBs (2°–15°) increased with the inclination from the build direction (i.e., higher in XY and ZX vs. *Z*), indicating the presence of substructure development due to thermal cycling and residual stress accumulation. These substructures contribute to strain hardening through dislocation entanglement, particularly in the XY and ZX orientations.

Upon tensile pre-deformation, the fraction of low-angle boundaries generally increased, particularly in the range of 2°–5°. For example, the XY specimen showed an increase from 22.9 to 24.3%, while the *Z*-oriented sample showed a slight reduction (26.5 to 16.0%). This trend suggests an orientation-dependent response to plastic deformation. While plastic strain in XY and ZX orientations activates recovery mechanisms leading to dislocation rearrangement and subgrain formation, the *Z*-oriented samples may experience grain fragmentation and boundary migration due to their columnar grain structure and higher defect density at interlayer regions.

Although prior studies (e.g., Casati et al. [28]) report minimal texture in LPBF 316L processed using a meander scanning strategy with inter-layer rotation, the yield surface asymmetry and anisotropic yield strength observed in the current study suggest that microstructural heterogeneity extends beyond texture alone. Subtle orientation clustering, remelted zones, and directional solidification phenomena—especially evident in the *Z*-oriented builds—introduce localized anisotropies even in the absence of strong crystallographic texture. The grain size and morphology, dictated by melt pool dynamics and remelting effects, result in directionally dependent mechanical properties. For instance, the higher strength observed in XY and ZX specimens can be attributed to finer, equiaxed grains that impede dislocation motion uniformly across loading directions [29, 32].

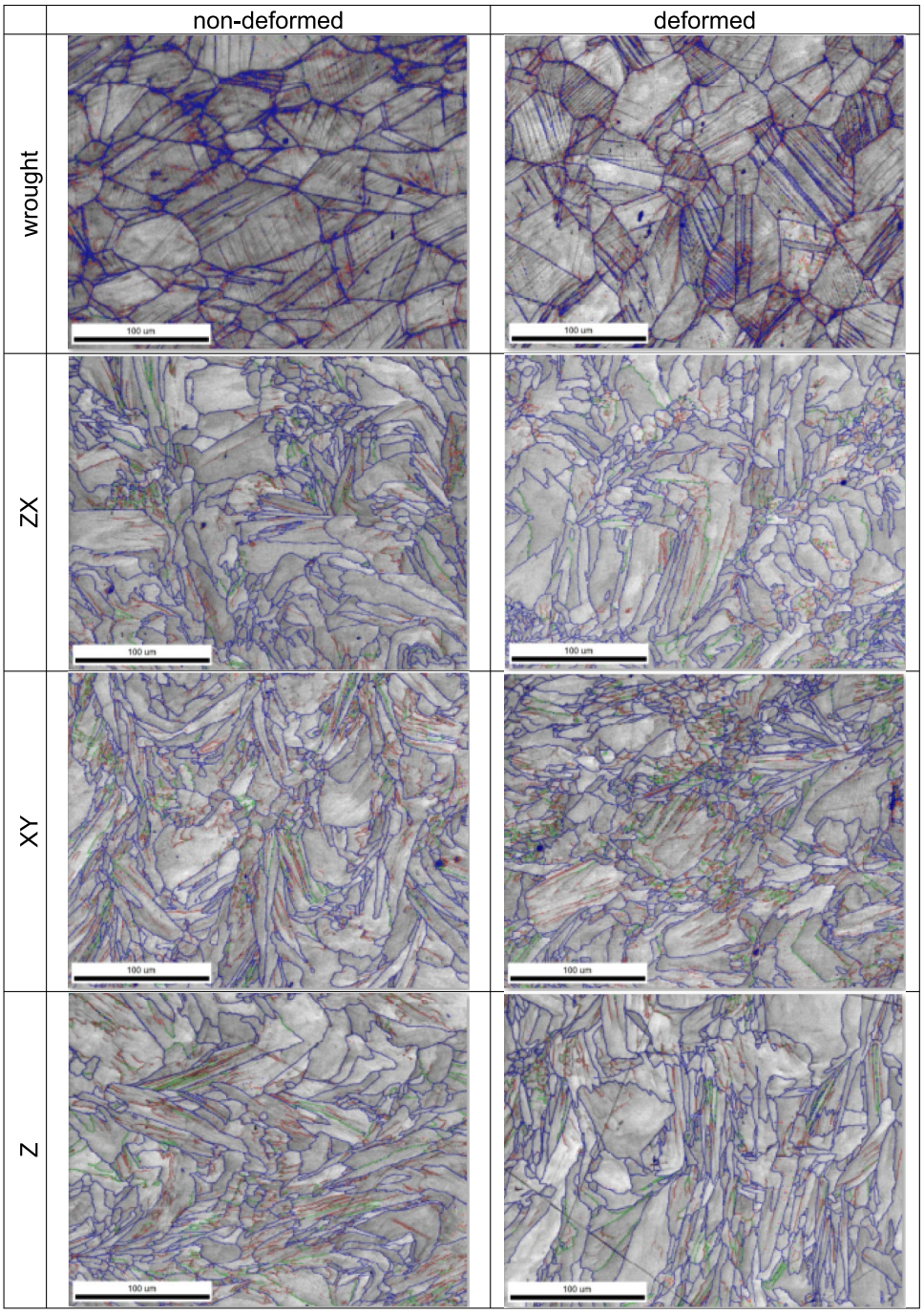

Fig. 11 Grain distribution maps of SS316L specimens

Table 5 Grain distribution values of tested SS316L specimens

	Wrought			ZX			XY			*Z*		
Misorientation angle	2°–5°	5°–15°	15°–180°	2°–5°	5°–15°	15°–180°	2°–5°	5°–15°	15°–180°	2°–5°	5°–15°	15°–180°
Non-deformed	0.280	0.031	0.689	0.181	0.084	0.734	0.229	0.117	0.654	0.265	0.137	0.598
Deformed	0.338	0.038	0.624	0.174	0.103	0.723	0.243	0.128	0.629	0.160	0.097	0.743

In contrast, in the *Z*-oriented samples, columnar grains and their alignment with the loading axis promote easier dislocation glide along specific crystallographic planes, contributing to earlier yielding and pronounced softening.

One can clearly observe that the yield surface shapes and their evolution with pre-strain are deeply influenced by the initial microstructure. Initial yield surfaces for XY and ZX samples were nearly symmetric and more closely resembled the Huber–von Mises–Hencky (HMH) isotropic criterion, consistent with their more equiaxed microstructures and lower degrees of anisotropy. These specimens also exhibited less rotation and distortion of the yield surface upon plastic pre-deformation, suggesting more uniform work hardening behaviour. On the other hand, the *Z*-oriented specimens demonstrated pronounced deviation from the isotropic yield locus. The centre of the yield surface for the *Z* specimen was significantly shifted along the compressive direction (Table 3), and a greater degree of softening was observed upon pre-straining.

This reflects the combined influence of the columnar grain structure, higher defect concentration at layer boundaries, and directional dislocation pile-up, all of which contribute to asymmetric plastic flow. The mechanical anisotropy quantified by axis ratios of the elliptical yield surfaces (1.44–1.58 for LPBF samples vs. 1.05 for wrought) was further confirmed during EBSD analysis. The greater the axis ratio, the more directional dependency is observed in yield behaviour—directly tied to microstructural anisotropy arising from AM processing [16, 30, 31]. Additionally, the evolution of yield surface shape and size with increasing pre-strain—particularly the rotation of the major axis—indicates a complex interaction between accumulated plastic strain and microstructural response. The LPBF samples, especially in XY orientation, showed a pronounced rotation (up to 0.79 radians) of the yield surface after 0.8% plastic strain, reflecting the activation of new slip systems and possible strong directional microstructural features induced by deformation.

4 Concluding remarks

This paper provides a comprehensive analysis of the mechanical behaviour of wrought SS316L and LPBF-printed SS316L in XY, ZX, and *Z* orientations, focusing on their yield surface evolution, strain-hardening mechanism, and anisotropic behaviour under tensile plastic pre-deformation. To the author's knowledge, there are no such prior studies available related to the experimental investigation of yield surface and its evolution reflecting prior deformation for additively manufactured SS316L. The yield surfaces were determined employing a single specimen approach and sequential probing technique for the plastic offset strain equal to 0.001% and 0.005%. Additionally, tensile plastic pre-deformation at 0.35%, 0.5%, and 0.8% plastic strain was introduced to all materials. The main findings can be summarized as follows:

- The layer-by-layer additive manufacturing process introduces directional dependencies in mechanical properties, affecting the strength, stiffness, and plasticity of the material. The *Z*-oriented specimens exhibit the lowest mechanical performance, primarily due to weaker interlayer bonding, while the XY and ZX orientations show relatively higher yield strength and more uniform hardening behaviour. The wrought SS316L shows the highest mechanical properties among all specimens.
- The loading–unloading cyclic behaviour in LPBF-printed SS316L is highly dependent on printing orientation, with wrought SS316L outperforming all LPBF orientations in terms of elastic recovery and reduced plastic strain accumulation. The findings emphasize the need for strategic part orientation in design, optimized post-processing, and predictive modelling of mechanical anisotropy for improving the structural reliability of additively manufactured components in high-cycle loading applications.
- The initial yield surfaces obtained at 0.005% plastic offset strain demonstrate that the yield strengths of LPBF-printed specimens were increased along the axial stress direction, but reduced along the shear stress one, in comparison to wrought SS316L. Such behaviour was associated with a certain form of material anisotropy representing different textures and crystal structures.
- The subsequent yield surfaces obtained at 0.001% plastic offset strain reflecting tensile plastic pre-strain exhibit softening of the wrought and LPBF-printed SS316L specimens. The degree of this effect depends on the material morphology and pre-strain level.
- The minimal discrepancies between experimental yield points and fitted yield surfaces show the ability of the Szczepinski yield function to capture the evolution of yield surfaces at different pre-strain levels. This signifies the utilization of precise mathematical approximations to characterize yield surfaces, particularly for anisotropic materials such as LPBF-printed SS316L, where microstructural variations contribute to directional differences in plasticity.
- EBSD observations confirmed that differences in grain morphology and crystallographic orientation, especially the presence of columnar grains in the *Z* direction and more equiaxed grains in the XY and ZX orientations, contribute significantly to the anisotropic yield behaviour and evolution of the yield surface in LPBF-processed SS316L.

Acknowledgements The authors would like to express their gratitude to Mr. M. Wyszkowski and Mr. A. Chojnacki for their kind help during the experimental part of this work.

Author contributions Conceptualization: M.K. and Z.K.; data curation: M.K. and V.P.D.; formal analysis: M.K., V.P.D., P.W. and Z.K.; investigation: M.K., D.P., M.P., P.W., and V.P.D.; methodology: M.K., D.P., P.W., M.P., and Z.K.; project administration: M.K., P.W.; supervision: M.K. and Z.K.; validation: M.K., P.W., Z.K.; visualization: M.K.; roles/writing—original draft: M.K. and V.P.D.; writing—review and editing: Z.K., P.W.

Funding This work was funded partly by the National Science Centre through the grant nos. 2019/35/B/ST8/03151 and 2023/51/B/ST8/01751.

Declarations

Competing interests The authors declare no competing interests.

References

1. Avanzini A (2022) Fatigue behavior of additively manufactured stainless steel 316L. Materials 16(1):65. https://doi.org/10.3390/ma16010065
2. Gor M, Soni H, Wankhede V, Sahlot P, Grzelak K, Szachgluchowicz I, Kluczyński J (2021) A critical review on effect of process parameters on mechanical and microstructural properties of powder-bed fusion additive manufacturing of SS316L. Materials 14(21):6527. https://doi.org/10.3390/ma14216527
3. Bedmar J, Riquelme A, Rodrigo P, Torres B, Rams J (2021) Comparison of different additive manufacturing methods for 316L stainless steel. Materials 14(21):6504. https://doi.org/10.3390/ma14216504
4. D'Andrea D (2023) Additive manufacturing of AISI 316L stainless steel: a review. Metals 13(8):1370. https://doi.org/10.3390/met13081370
5. Khalid M, Peng Q (2021) Investigation of printing parameters of additive manufacturing process for sustainability using design of experiments. J Mech Des 143(3):032001. https://doi.org/10.1115/1.4049521
6. Santonocito D, Fintová S, Di Cocco V, Iacoviello F, Risitano G, D'Andrea D (2023) Comparison on mechanical behavior and microstructural features between traditional and AM AISI 316L. Fatigue Fract Eng Mater Struct 46(2):379–395. https://doi.org/10.1111/ffe.13872
7. Elambasseril J, Rogers J, Wallbrink C, Munk D, Leary M, Qian M (2023) Laser powder bed fusion additive manufacturing (LPBF-AM): the influence of design features and LPBF variables on surface topography and effect on fatigue properties. Crit Rev Solid State Mater Sci 48(1):132–168. https://doi.org/10.1080/10408436.2022.2041396
8. Alsalla HH, Smith C, Hao L (2018) Effect of build orientation on the surface quality, microstructure and mechanical properties of selective laser melting 316L stainless steel. RPJ 24(1):9–17. https://doi.org/10.1108/RPJ-04-2016-0068
9. Smith TR, Sugar JD, San Marchi C, Schoenung JM (2017) Orientation effects on fatigue behavior of additively manufactured stainless steel, Volume 6A: Materials and fabrication, American Society of Mechanical Engineers, Waikoloa, Hawaii, USA, p. V06AT06A020. https://doi.org/10.1115/PVP2017-65948
10. Yang N, Yee J, Zheng B, Gaiser K, Reynolds T, Clemon L, Lu WY, Schoenung JM, Lavernia EJ (2017) Process-structure-property relationships for 316L stainless steel fabricated by additive manufacturing and its implication for component engineering. J Therm Spray Tech 26(4):610–626. https://doi.org/10.1007/s11666-016-0480-y
11. Guo P, Zou B, Huang C, Gao H (2017) Study on microstructure, mechanical properties and machinability of efficiently additive manufactured AISI 316L stainless steel by high-power direct laser deposition. J Mater Process Technol 240:12–22. https://doi.org/10.1016/j.jmatprotec.2016.09.005
12. Kowalewski ZL (1997) Assessment of cyclic properties of 18G2A low-alloy steel at biaxial stress state. Acta Mech 120(1):71–89. https://doi.org/10.1007/BF01174317
13. Kowalewski ZL, Śliwowski M (1997) Effect of cyclic loading on the yield surface evolution of 18G2A low-alloy steel. Int J Mech Sci 39(1):51–68. https://doi.org/10.1016/0020-7403(96)00016-1
14. Lavery NP, Cherry J, Mehmood S, Davies H, Girling B, Sackett E, Brown SGR, Sienz J (2017) Effects of hot isostatic pressing on the elastic modulus and tensile properties of 316L parts made by powder bed laser fusion. Mater Sci Eng A 693:186–213. https://doi.org/10.1016/j.msea.2017.03.100
15. Kumar P, Jayaraj R, Suryawanshi J, Satwik UR, McKinnell J, Ramamurty U (2020) Fatigue strength of additively manufactured 316L austenitic stainless steel. Acta Mater 199:225–239. https://doi.org/10.1016/j.actamat.2020.08.033
16. Somlo K, Frodal BH, Funch CV, Poulios K, Winther G, Hopperstad OS, Børvik T, Niordson CF (2022) Anisotropic yield surfaces of additively manufactured metals simulated with crystal plasticity. Eur J Mech A-Solids 94:104506. https://doi.org/10.1016/j.euromechsol.2022.104506
17. Wang H, Shu X, Zhao J, Alexandrov IV (2023) Biaxial tensile behavior of stainless steel 316L manufactured by selective laser melting. Sci Rep 13(1):21925. https://doi.org/10.1038/s41598-023-49482-7
18. Kořínek M, Halama R, Fojtík F, Pagáč M, Krček J, Krzikalla D, Kocich R, Kunčická L (2020) Monotonic tension-torsion experiments and FE modeling on notched specimens produced by SLM technology from SS316L. Materials 14(1):33. https://doi.org/10.3390/ma14010033
19. Szczepinski W (1993) On deformation-induced plastic anisotropy of sheet metals. Arch Mech 45(1):3–38
20. Wood P, Libura T, Kowalewski ZL, Williams G, Serjouei A (2019) Influences of horizontal and vertical build orientations and post-fabrication processes on the fatigue behavior of stainless steel 316L produced by selective laser melting. Materials 12(24):4203. https://doi.org/10.3390/ma12244203
21. Sasikumar R, Kannan AR, Kumar SM, Pramod R, Kumar NP, Shanmugam NS, Palguna Y, Sivankalai S (2022) Wire arc additive manufacturing of functionally graded material with SS 316L and IN625: microstructural and mechanical perspectives. CIRP J Manuf Sci Technol 38:230–242. https://doi.org/10.1016/j.cirpj.2022.05.005

22. Wang C, Tan X, Liu E, Tor SB (2018) Process parameter optimization and mechanical properties for additively manufactured stainless steel 316L parts by selective electron beam melting. Mater Des 147:157–166. https://doi.org/10.1016/j.matdes.2018.03.035
23. Aversa A, Saboori A, Librera E, de Chirico M, Biamino S, Lombardi M, Fino P (2020) The role of directed energy deposition atmosphere mode on the microstructure and mechanical properties of 316L samples. Addit Manuf 34:101274. https://doi.org/10.1016/j.addma.2020.101274
24. Benjamin D, Kirkpatrick CW (1980) ASM metals handbook, properties and selection: stainless steels, tool materials and special-purpose metals, vol 3, 9th edn. Met. Handbook. American Society of Metals
25. Thijs L, Kempen K, Kruth J-P, Van Humbeeck J (2013) Fine-structured aluminium products with controllable texture by selective laser melting of pre-alloyed AlSi10Mg powder. Acta Mater 61(5):1809–1819. https://doi.org/10.1016/j.actamat.2012.11.052
26. Thijs L, Montero Sistiaga ML, Wauthle R, Xie Q, Kruth J-P, Van Humbeeck J (2013) Strong morphological and crystallographic texture and resulting yield strength anisotropy in selective laser melted tantalum. Acta Mater 61(12):4657–4668. https://doi.org/10.1016/j.actamat.2013.04.036
27. Salman OO, Brenne F, Niendorf T, Eckert J, Prashanth KG, He T, Scudino S (2019) Impact of the scanning strategy on the mechanical behavior of 316L steel synthesized by selective laser melting. J Manuf Process 45:255–261. https://doi.org/10.1016/j.jmapro.2019.07.010
28. Casati R, Lemke J, Vedani M (2016) Microstructure and fracture behavior of 316L austenitic stainless steel produced by selective laser melting. J Mater Sci Technol 32(8):738–744. https://doi.org/10.1016/j.jmst.2016.06.016
29. Mertens A, Reginster S, Paydas H, Contrepois Q, Dormal T, Lemaire O, Lecomte-Beckers J (2014) Mechanical properties of alloy Ti–6Al–4V and of stainless steel 316L processed by selective laser melting: influence of out-of-equilibrium microstructures. Powder Metall 57(3):184–189. https://doi.org/10.1179/1743290114Y.0000000092
30. Charmi A, Falkenberg R, Ávila L, Mohr G, Sommer K, Ulbricht A, Sprengel M, Saliwan Neumann R, Skrotzki B, Evans A (2021) Mechanical anisotropy of additively manufactured stainless steel 316L: an experimental and numerical study. Mater Sci Eng A 799:140154. https://doi.org/10.1016/j.msea.2020.140154
31. Kumar D, Shankar G, Prashanth KG, Suwas S (2024) Control of texture and microstructure in additive manufacturing of stainless steel 316 L. J Alloys Compd 976:173040. https://doi.org/10.1016/j.jallcom.2023.173040
32. Liu Z, Yang Y, Xiao Y, Lei H, Yang C, Liu Z, Zhao Q, Song C (2024) Investigation of 316L microstructure evolution mechanism and mechanical properties in dual-laser powder bed fusion with controllable remelting time interval. Mater Des 239:112761. https://doi.org/10.1016/j.matdes.2024.112761
33. Wang J, Zhu R, Liu Y, Zhang L (2023) Understanding melt pool characteristics in laser powder bed fusion: an overview of single- and multi-track melt pools for process optimization. Advanced Powder Materials 2(4):100137. https://doi.org/10.1016/j.apmate.2023.100137
34. Iqbal N, Jimenez-Melero E, Ankalkhope U, Lawrence J (2019) Microstructure and mechanical properties of 316L stainless steel fabricated using selective laser melting. MRS Adv 4(44–45):2431–2439. https://doi.org/10.1557/adv.2019.251
35. Khan AS, Kazmi R, Pandey A, Stoughton T (2009) Evolution of subsequent yield surfaces and elastic constants with finite plastic deformation. Part-I: a very low work hardening aluminum alloy (Al6061-T6511). Int J Plast 25(9):1611–1625. https://doi.org/10.1016/j.ijplas.2008.07.003
36. Khan AS, Pandey A, Stoughton T (2010) Evolution of subsequent yield surfaces and elastic constants with finite plastic deformation. Part II: a very high work hardening aluminum alloy (annealed 1100 Al). Int J Plast 26(10):1421–1431. https://doi.org/10.1016/j.ijplas.2009.07.008
37. Ishikawa H (1997) Subsequent yield surface probed from its current center. Int J Plast 13(6):533–549. https://doi.org/10.1016/S0749-6419(97)00024-7
38. Motaman SAH, Roters F, Haase C (2020) Anisotropic polycrystal plasticity due to microstructural heterogeneity: a multi-scale experimental and numerical study on additively manufactured metallic materials. Acta Mater 185:340–369. https://doi.org/10.1016/j.actamat.2019.12.003
39. Agius D, Wallbrink C, Kourousis KI (2021) Efficient modelling of the elastoplastic anisotropy of additively manufactured Ti-6Al-4V. Addit Manuf 38:101826. https://doi.org/10.1016/j.addma.2020.101826
40. Wilson-Heid AE, Qin S, Beese AM (2018) Anisotropic multiaxial plasticity model for laser powder bed fusion additively manufactured Ti-6Al-4V. Mater Sci Eng A 738:90–97. https://doi.org/10.1016/j.msea.2018.09.077